remote sensing

MDPI

Article

Internal Tides and Their Intraseasonal Variability on the Continental Slope Northeast of Taiwan Island Derived from Mooring Observations and Satellite Data

Yuqi Yin [1,2,3,*], Ze Liu [1,2,3], Yuanzhi Zhang [4], Qinqin Chu [5], Xihui Liu [6], Yijun Hou [1,2,3,7] and Xinhua Zhao [8]

1 CAS Key Laboratory of Ocean Circulation and Waves, Institute of Oceanology, Chinese Academy of Sciences, Qingdao 266071, China; liuze@qdio.ac.cn (Z.L.); yjhou@qdio.ac.cn (Y.H.)
2 Pilot National Laboratory for Marine Science and Technology (Qingdao), Qingdao 266200, China
3 Center for Ocean Mega-Science, Chinese Academy of Sciences, Qingdao 266071, China
4 School of Marine Science, Nanjing University of Information Science and Technology, Nanjing 210044, China; yuanzhizhang@cuhk.edu.hk
5 QHD Marine Environmental Central Station of SOA, Qinhuangdao 066002, China; chuqinqin@ncs.mnr.gov.cn
6 China National Environmental Monitoring Centre, Beijing 100012, China; liuxh@cnemc.cn
7 University of Chinese Academy of Sciences, Beijing 100049, China
8 Jiangsu Marine Resources Development Research Institute, Jiangsu Ocean University, Lianyungang 222005, China; zhaoxinhua@jou.edu.cn
* Correspondence: yinyuqi@qdio.ac.cn; Tel.: +86-532-82898516

Abstract: In this study, strong internal tides were observed on the continental slope northeast of Taiwan Island. Owing to the lack of long-term observations, these tides' intraseasonal variability and the impact of the Kuroshio Current remain unclear. This study aimed to fill in the gaps using one-year continuous mooring observations, satellite data and analysis data. The horizontal kinetic energy (HKE) of semidiurnal internal tides showed that there was conspicuous energy from 100 days to 200 days, which was mainly attributed to the cross-term of HKE. The impact of the Kuroshio Current and mesoscale eddies on the HKEs were assessed: Cyclonic (anticyclonic) mesoscale eddies propagated from the open ocean, weakened (strengthened) the Kuroshio and shifted the Kuroshio onshore (offshore) northeast of Taiwan Island. The weakened (strengthened) Kuroshio increased (decreased) the shoreward velocity at the mooring site, and the onshore (offshore) Kuroshio migration increased (decreased) the northeastward velocity and enhanced (weakened) the HKEs of internal tides by modulating the tidal energy horizontal propagation. The weakened (strengthened) Kuroshio also resulted in gentler (steeper) isopycnals across the slope and enhanced (weakened) the HKEs of internal tides by influencing the interaction between ocean stratification and bottom topography.

Keywords: internal tides; Kuroshio Current; intraseasonal; acoustic doppler current profiler (ADCP); mesoscale eddy

Citation: Yin, Y.; Liu, Z.; Zhang, Y.; Chu, Q.; Liu, X.; Hou, Y.; Zhao, X. Internal Tides and Their Intraseasonal Variability on the Continental Slope Northeast of Taiwan Island Derived from Mooring Observations and Satellite Data. *Remote Sens.* **2022**, *14*, 59. https://doi.org/10.3390/rs14010059

Academic Editor: Jorge Vazquez

Received: 21 November 2021
Accepted: 21 December 2021
Published: 23 December 2021

1. Introduction

Internal tides, which are generated in stratified waters through the interaction of barotropic tides and varying bathymetry, such as shelf breaks, ridges, sills and submarine canyons [1–3], are widely distributed in oceans. The vertical structure of internal tides is very complex, and current shear tends to induce intense instability, turbulence and diapycnal mixing [4–6]. Therefore, internal tides play an important role in maintaining ocean stratification and meridional overturning circulation, as well as energy redistribution [7,8]. In addition, internal tides also pose hazards for acoustic transmission and underwater navigation [9]. Further study of internal tides, including of their generation, propagation and dissipation, can improve numerical simulations and understanding of the dynamic ocean environment.

The observation of internal tides can be traced back to the early nineteenth century, and the linear theoretical model for internal tide generation has been in use since it was

developed in the 1960s [1,10]. Benefitting from satellite and computer technology, global observations and high-resolution numerical simulations provide strong support to the investigation of internal tides. Generally, after generation, first-mode internal tides radiate away and can propagate thousands of kilometers, while higher-mode internal tides break near the generation sites [11–13]. During the propagation of low-mode internal tides, they interact with each other, which leads to linear/nonlinear wave–wave interaction. Further, they also interact with bottom topography or other ocean dynamic processes that induce wave scattering [14,15]. In the meantime, energy is transferred to the smaller scale. Once the shear of the baroclinic current induced by the internal tides is strong enough, diapycnal mixing occurs [5–7,12].

In the western Pacific, the Luzon Strait and the East China Sea shelf break are characterised by major generation regions of internal tides [16–18]. The steep continental shelf slope around the western boundary is the main cause of these. In addition, the strong western boundary currents enhance vertical stratification on their left-hand side, which results in more internal tide energy. While the East China Sea shelf break is far from the coast, its barotropic tides are still strong. The velocity of the M_2 tide current is approximately 20 cm s^{-1} during high tides, while that of the K_1 tide current is approximately 5 cm s^{-1} [19–21]. Moreover, tidal currents are predominantly in the cross-slope direction [22], which favours internal tide generation. Early in situ temperature and current observations, synthetic aperture radar (SAR) and ocean colour images [23] have proven the existence of internal tides. Using an underwater sliding vehicle, internal tides and their vertical structures were observed along two sections across the shelf break during autumns from 1986 to 1989 [24]. The generation and propagation of internal tides on the continental slope northeast of Taiwan Island are characterised by data from an array of subsurface moorings [25,26]. Semidiurnal tides are stronger than diurnal tides, and the M_2 tide is the dominant semidiurnal internal constituent. The semidiurnal tides show slow a propagation speed and strong vertical shear, which could trigger shear instability, dissipate and provide turbulence mixing. The semidiurnal tidal energy flux forced by the M_2 tide propagates predominantly seaward. Using satellite SAR images, rank-ordered packets of nonlinear internal waves in the East China Sea are also often observed, especially in northeastern Taiwan Island [27,28]. These complicated internal waves could be generated by upwelling, which has been found to be induced by the Kuroshio onshore intrusion across the continental shelf. The Mien-Hua Canyon and the north shelf are considered to be the energetic sources of M_2 internal tides [3].

In addition to astronomical forcing, the variations in internal tide generation, evolution and energy flux are influenced by water stratification and background currents [1,29]. Coherent internal tides are phase-locked with barotropic tides at the generation site, while the residual of the internal tides is the incoherent component [30,31]. Coherent internal tides have been found to show weak dissipation [13], while incoherent internal tides could induce strong current shear, which plays an important role in cascading tidal energy to turbulent mixing [8,32,33]. Decomposition analysis has provided better understanding of internal tides, as well as the influence of background stratification and currents.

Because in situ measurements along the East China Sea shelf break are limited, studies on variations in internal tides and their mechanisms are insufficient. However, there are some relevant studies that took place in the northwestern South China Sea. The notable seasonal variability in internal tides on the continental slope of the northwestern South China Sea has been attributed to upper ocean stratification variation [34]. Both observational data and numerical simulations have captured the seasonal and interannual variability in internal tide energy associated with the Kuroshio [35–37]. The amplitude of the generated M_2 internal tides was found to increase by about 11% with the Kuroshio intrusion. The thermocline interface could modulate the interaction between the strong jet and bottom topography [38]. The strengthened (weakened) Kuroshio forces the interface to become more parallel (perpendicular) to the eastern (western) flank of the ridge in the Luzon Strait, resulting in a weakened (strengthened) interaction between stratification and

bottom topography [39]. Considering the effect of energy advection and lateral friction, the influence of the Kuroshio location on the baroclinic energy flux of the internal tide was also discussed. In addition, Yuan et al. [40] suggested a western boundary current instability generation mechanism was responsible for the internal waves in the Luzon Strait.

Abundant internal tides are generated in the Luzon Strait, and the evolution of its internal tides is affected by the background current and stratification associated with mesoscale eddies. Numerical studies have shown that mesoscale eddies can redistribute the energy of internal solitary waves along their wave fronts due to retardation and acceleration effects [41]. Anticyclonic eddies have been found to increase the incoherency of internal tides by affecting both their amplitudes and phases [42]. Li et al. [37] suggested that mesoscale eddies on the path of internal tides can substantially distort the propagation paths of internal tides, which can lead to remarkable variation in the amplitude of internal tides at a fixed location. Using in situ velocity observation west of Luzon Strait, Huang et al. [43] revealed that with an anticyclonic eddy, the amplitudes of internal tides significantly decreased due to thermocline deepening along the wave direction, and both thermocline deepening and eddy currents accelerated the propagation of internal tides. The tidal beam propagation in the deep basin between the Luzon Strait and the northern South China Sea continental shelf affects the intraseasonal variation in tidal energy flux on the shelf [44].

In the northeastern region of Taiwan Island, strong internal tides are well known. However, in situ data, especially long-term observations that present the intraseasonal and seasonal variabilities in internal tides, are still sparse. Additionally, there is also a strong western boundary current and its onshore intrusion, and both are highly modulated by open ocean mesoscale eddies [45–48]. The relationship between these factors and the internal tides and the mechanisms behind them remain unclear. In this study, one-year continuous current observations on the slope northeast of Taiwan Island provided a valuable opportunity to estimate the long-term variability in internal tides. Using tidal harmonic analysis, the characteristics of the internal tides and their temporal-spatial variability were revealed. By combining the satellite remote sensing data and ocean analysis data, the impacts of the Kuroshio Current and mesoscale eddies, as well as their mechanisms were further discussed.

2. Data and Methods

2.1. In Situ Velocities

A mooring for measuring in situ velocities was constructed on the slope northeast of Taiwan Island, which provided strong support for the study of the impact of Kuroshio Current on the regional ocean dynamics around the shelf break. The mooring station was 122°35.8′ E, 25°30.3′ N (Figure 1), located at 600 m and configured with an up-looking 75 kHz ADCP at 500 m. We obtained a continuous velocity time series from 23 May 2017 to 19 May 2018, which was accomplished within three cruises. On 19 September 2017, the mooring was recovered and redeployed for the battery replacement of ADCP. The vertical resolution of the velocity was 8 m. The near surface velocities which were interfered with by sidelobe reflections were abandoned, and the remaining velocities covered ranges from 46 m to 478 m. The current velocity was sampled per hour.

2.2. Satellite Altimetry Data

Gridded sea level heights and currents were introduced to estimate the Kuroshio Current and reveal the sea surface height variation east of Taiwan Island. Satellite data were processed from all available altimeter missions. The data resolution was $1/4^\circ \times 1$ day, which enabled us to distinguish mesoscale eddies [49] and ocean currents [46,47] easily. Sea level anomalies were calculated with respect to the mean sea surface from 1993 to 2012 [50]. The sea surface geostrophic velocities were derived from the sea level based on the geostrophic balance.

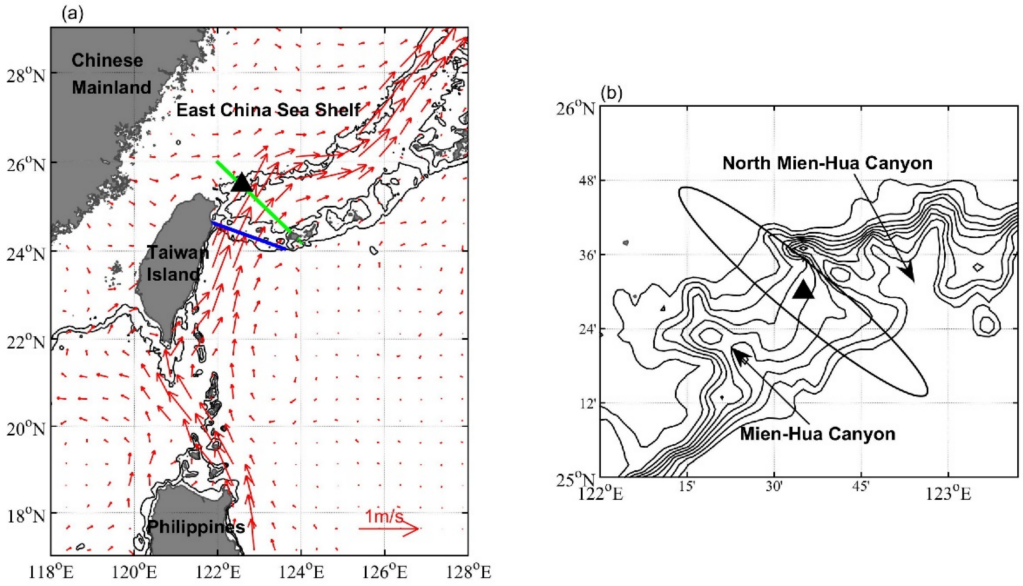

Figure 1. (**a**) Mean geostrophic velocities (red arrows, from satellite altimetry data). The blue line represents the East Taiwan Channel (ETC) transect, and the green line represents the P transect. Thin contours are the 200 m and 1000 m isobaths (ETOPO1 Global Relief Model). The mooring location is labeled as the black triangle. (**b**) Detailed topography around the mooring station. Thin contours are the isobaths every 100 m from 200 m to 1000 m. The M_2 tidal ellipse is shown.

2.3. Ocean Analysis Data

Since there was not synchronous temperature and salinity profile observation, the analysis data generated by the data assimilative global Hybrid Coordinate Ocean Model (HYCOM; [51]) was introduced to depict the ocean stratification variation during mooring observations. The HYCOM uses the Navy Coupled Ocean Data Assimilation (NCODA) system [52] and assimilates multi-source data, including satellite data (e.g., sea surface level and temperature), and in situ temperature and salinity observations, and profiles from XBTs, Argo floats and moored buoys. The data resolution was $1/12^\circ \times 1$ day, and there was 40 z-levels. Tides were not included in the model.

2.4. Tidal Harmonic Analyses

In this study, eight major diurnal (K_1, O_1, P_1 and Q_1) and semidiurnal (M_2, S_2, N_2 and K_2) constituents were derived from harmonic analyses of currents over the whole observation period:

$$V = \sum_n U_n \cos(\psi_n + \omega_n t) \quad (1)$$

where U_n is the amplitude, ψ_n is the phase, and ω_n is the frequency of each constituent.

3. Results

A rotary spectral analysis was performed on the current velocity. The depth-averaged rotary spectra of raw currents indicated that the semidiurnal tidal signal was dominant at the mooring station, while the diurnal tidal signal had a secondary influence (Figure 2). This finding suggested that the semidiurnal internal tide was much stronger than the diurnal tide. The clockwise component of the rotary spectra was comparable with the counterclockwise component, with the clockwise component being slightly larger. There were also significant spectral peaks around frequencies of 3 cpd (cycle per day, O_1 + M_2) and 4 cpd (M_4). In addition, the near inertial waves also had abundant energy in the upper layer (46–94 m) and showed a peak at 0.75 cpd (not shown here).

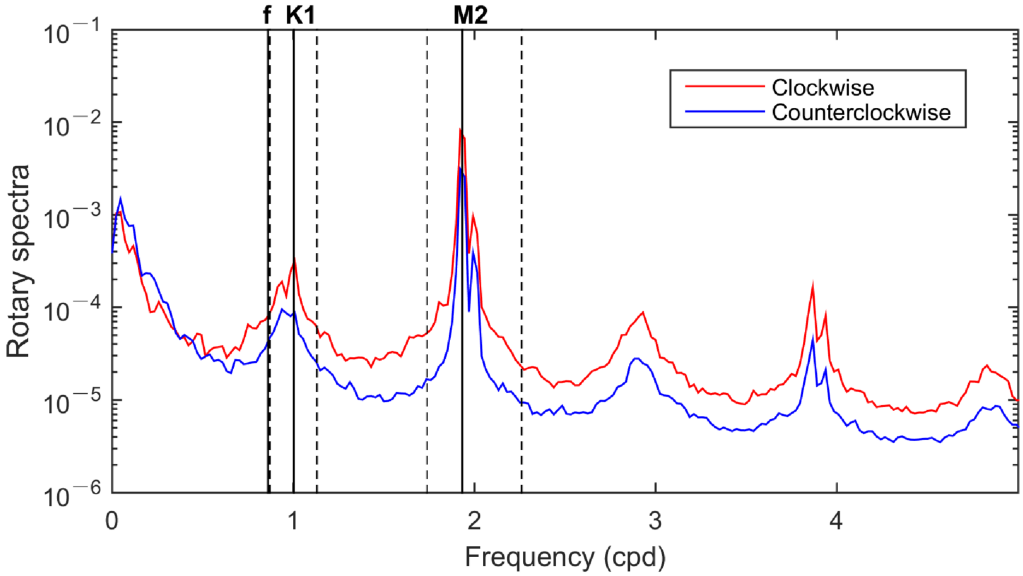

Figure 2. Depth-averaged rotary spectra (unit: $m^2\ s^{-2}$) for clockwise and counterclockwise components of raw velocity at the mooring station. The dashed lines represent the frequency bands of 0.87–1.13 and 1.74–2.26 cpd.

3.1. Barotropic Tides

Harmonic analyses were performed on the depth-averaged velocities ($\overline{u}, \overline{v}$), and the principal tidal constituents were extracted. Barotropic tidal currents at the mooring station were dominated by the semidiurnal constituents M_2 and S_2 (Table 1, Figure 3a). The diurnal constituents were much weaker than the semidiurnal constituents, which was consistent with the rotary spectra of velocities. M_2 was the largest barotropic tidal constituent, recording an amplitude of 24.12 cm s^{-1}. The amplitude of the S_2 current ellipse was about one-third that of M_2, and the amplitude of the K_1 current ellipse was one-thirteenth that of M_2. The mean angle of the isobaths (between 200 m and 1000 m) around the mooring station was approximately 50° from the north, while the mean inclination of the eight constituents was 134.5° from the east. Therefore, the barotropic tides were generally consistent with the cross-isobath direction within 4.5°. The tidal ellipse of the M_2 constituent, which was almost rectilinear, is shown in Figure 1b.

Table 1. Ellipse properties of eight major barotropic tidal constituents.

Constituents	K_1	O_1	P_1	Q_1	M_2	S_2	N_2	K_2
Amplitude (cm s^{-1})	1.86	1.27	0.44	0.38	24.12	7.47	4.11	1.78
Phase (°)	115	75	135	50	185	226	154	230
Inclination (°)	133	125	129	124	140	138	141	146

In general, the mean current flowed northward in the upper layer, showed an anticlockwise rotation with depth, and flowed southwestward from 182 m to 478 m [48]. After removing the eight barotropic tidal constituents, the residual depth-averaged velocities were estimated, which are shown in Figure 3b. Generally, the velocity was southwestward before 27 October 2017, and northwestward after 27 October 2017. Since the observation was very close to the Kuroshio, the current here was greatly influenced by the Kuroshio. Because of the local monsoon and seasonal heat flux, the Kuroshio Current shifts onshore in cold seasons and offshore in warm seasons, which strengthens the northward Kuroshio intrusion in winter and weakens the intrusion in summer [53,54]. It is worth noting that there were also intraseasonal variations, which should be induced by the intraseasonal variation in the Kuroshio intrusion, which is induced by mesoscale eddies from the open ocean [46–48].

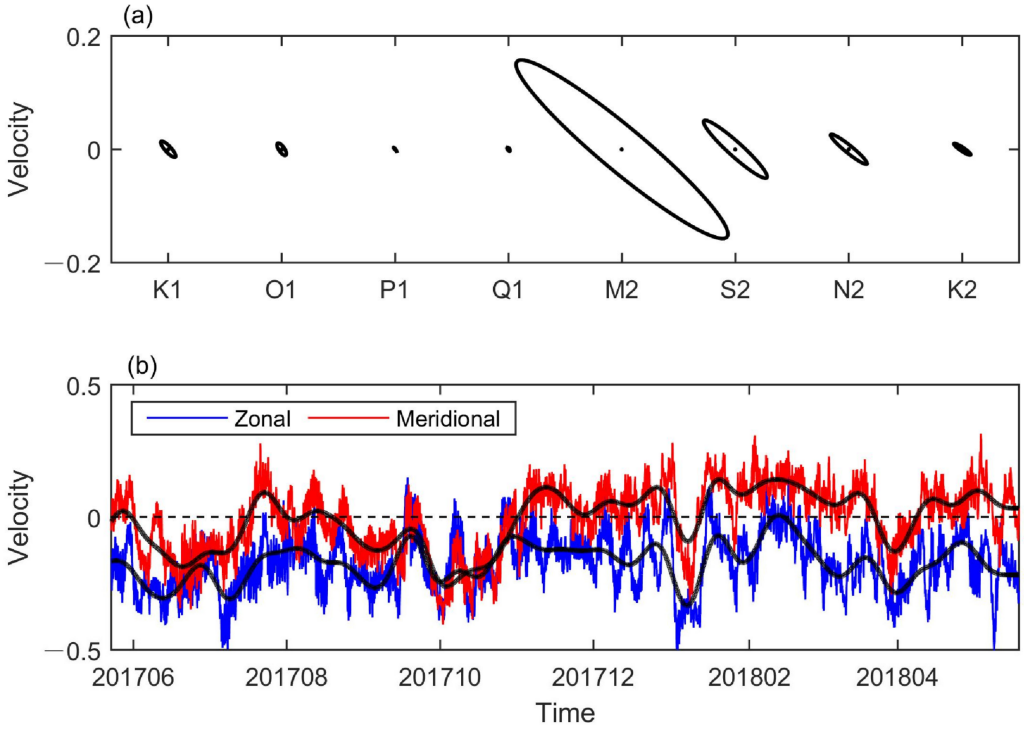

Figure 3. (**a**) Tidal ellipses of eight diurnal and semidiurnal barotropic tidal constituents. (**b**) Residual (after removing the tides) depth-averaged velocities; thick lines are the 20-day low-pass filtered velocities. (unit: m s^{-1}).

3.2. Internal Tides

Since the velocities were observed at the steep slope, and the barotropic tides were generally aligned with the cross-isobath direction, internal tides at the mooring station were strongly predictable. First, baroclinic velocities (u_0', v_0') were derived by subtracting the depth-averaged velocities from the raw data (u, v) at each depth:

$$u_0' = u - \overline{u}, \tag{2}$$

$$v_0' = v - \overline{v} \tag{3}$$

Then, to estimate the vertical distribution and temporal variability in internal tides (u', v') at the mooring station, a fourth-order Butterworth filter was applied to the baroclinic velocities. The Butterworth filter is a type of signal processing filter designed to have a frequency response as flat as possible in the passband. The fourth order corresponds to the larger steepness of the transfer characteristics from the passband to the topband, which makes the filter more selective. Diurnal currents were isolated with a bandpass filter of 0.87–1.13 cpd, while semidiurnal currents were isolated with a bandpass filter of 1.74–2.26 cpd (dashed lines in Figure 2).

Due to the variation in the ocean stratification and current field, the phase speeds of internal tide waves vary during their propagation, which induces the difference between observed internal tide waves and astronomical tide waves in phase. The internal tides were decomposed into coherent and incoherent components [30,31]. The tide signal purely determined by the astronomical forcing was considered to be a coherent tide (u_c', v_c'), while the remaining part was considered to be an incoherent tide (u_i', v_i'):

$$u' = u_c' + u_i', \tag{4}$$

$$v' = v_c' + v_i'. \tag{5}$$

In this study, the coherent internal tidal currents comprised eight major tidal constituents derived from harmonic analyses of baroclinic currents over the whole observational period. The semidiurnal internal tides were stronger than the diurnal ones (Figure 4). Similarly, the diurnal internal tides were dominated by K_1 and O_1, while the semidiurnal internal tides were dominated by M_2 and S_2. The depth-averaged amplitudes of K_1, O_1, M_2 and S_2 were 2.45 cm s^{-1}, 1.62 cm s^{-1}, 10.77 cm s^{-1} and 3.27 cm s^{-1}, respectively. On the whole, the amplitudes of the four constituents were largest at 46 m and first decreased and then increased with depth. In addition, the other maximum amplitude was recorded in the subsurface layer.

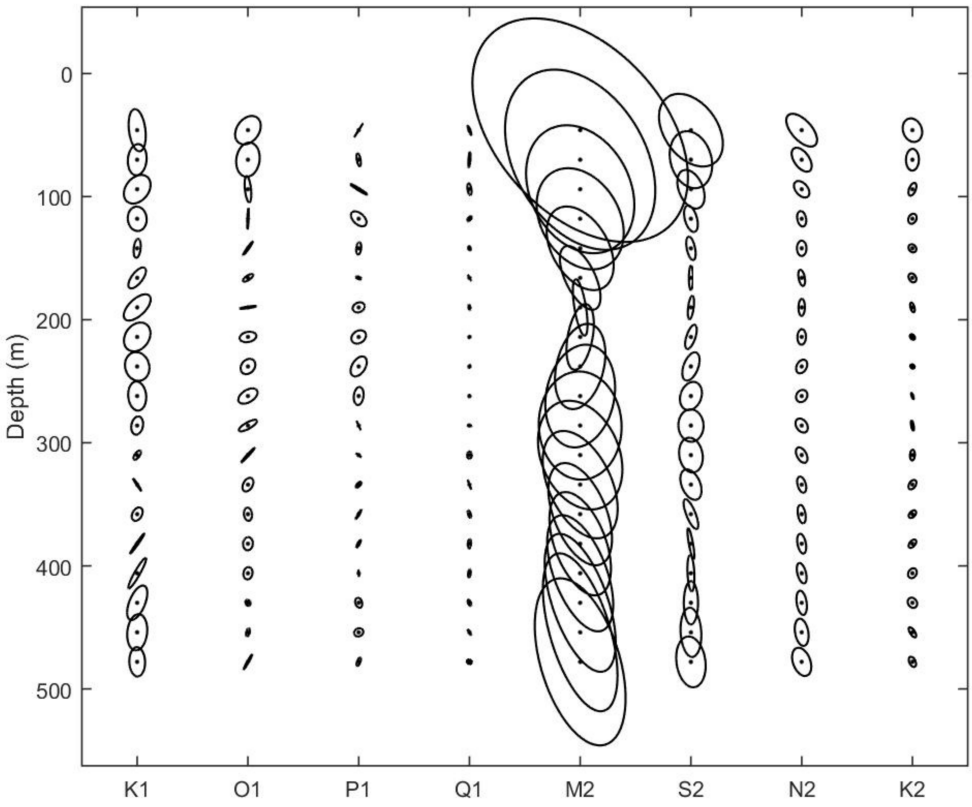

Figure 4. Tidal ellipses of eight baroclinic tidal constituents in different layers.

The M_2 tide was still the strongest tidal constituent. The amplitude of this tidal constituent was largest (23.66 cm s^{-1}) at 46 m, decreased to 5.2 cm s^{-1} at 190 m and increased to 15.6 cm s^{-1} at 478 m. The second minimum was 9.65 cm s^{-1} at 374 m. The ratio of the long axis to the short axis of M_2 mostly ranged from 1.3 to 2.7, and this ratio was able to reach 5 at 190 m. The inclination of M_2 was relatively stable above 126 m (~121.21°) and below 318 m (~110.62°). However, the inclination rapidly decreased from 121.76° at 126 m to 75.43° at 230 m, and increased to 115.57° at 318 m.

The horizontal kinetic energy (HKE) of the internal tides in each layer was defined as $\frac{1}{2}\rho_0\langle u'^2 + v'^2\rangle dz$. The HKE was composed of the coherent component (HKE_c), incoherent component (HKE_i) and cross-term (HKE_{cr}), which were given as follows:

$$HKE = HKE_c + HKE_i + HKE_{cr}, \tag{6}$$

$$HKE_c = \frac{1}{2}\rho_0\langle u_c'^2 + v_c'^2\rangle dz, \tag{7}$$

$$HKE_i = \frac{1}{2}\rho_0\langle u_i'^2 + v_i'^2\rangle dz, \tag{8}$$

$$HKE_{cr} = \rho_0\langle u_c'u_i' + v_c'v_i'\rangle dz. \tag{9}$$

where ρ_0 was considered to be constant (1024 kg m^{-3}), dz was the layer thickness and the bracket denoted the average over one tidal cycle [55]. The cross-term represents the HKE associated with the time-varying interference of incoherent currents, and its sign depends on the angle between the coherent and incoherent currents. The total, coherent component, incoherent component and cross-term HKEs of diurnal and semidiurnal internal tides were estimated (Figures 5 and 6). The ratio between the total HKEs of the diurnal and semidiurnal internal tides was 23.92%, while the ratios were 7.43% and 51.52% for the coherent and incoherent components, respectively. Therefore, the difference between the HKEs of the diurnal and semidiurnal internal tides was mostly due to the coherent component. The coherent component of the diurnal internal tides accounted for 19.45% of diurnal motions, while the coherent component of the semidiurnal internal tides accounted for 62.6% of semidiurnal motions. The incoherent component also made an important contribution to the internal tidal signal, especially for the diurnal internal tide.

The HKEs were largest at ~50 m for both diurnal and semidiurnal currents and decreased rapidly with depth from 50 m to 100 m (Figure 7). For the diurnal currents, both the total HKE and its incoherent component decreased slowly under 100 m. For semidiurnal currents, both the total HKE and its incoherent component decreased with depth, reached the minimum at ~200 m and then increased from 200 m to 478 m. The vertical distribution of the HKE coherent component was similar to the amplitude of the four major constituents. The coherent component of HKE for diurnal internal tides showed a subsurface maximum at ~230 m, while that of the semidiurnal internal tides was at ~300 m.

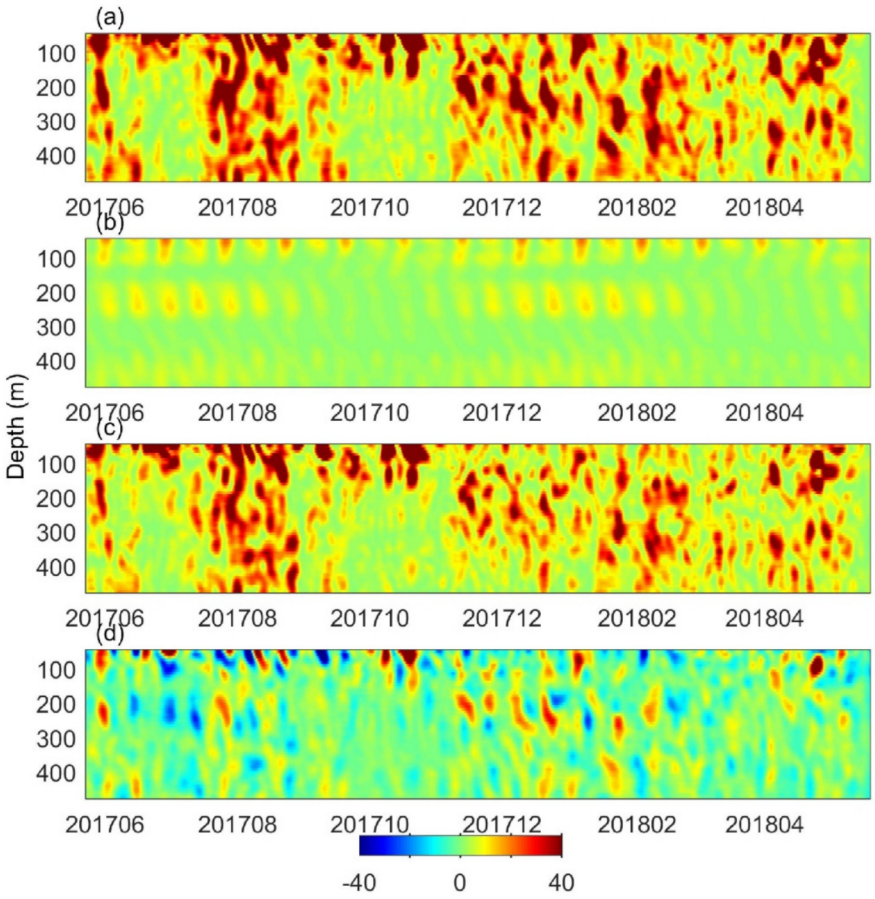

Figure 5. The horizontal kinetic energy values (HKEs; unit: J m^{-1}) of diurnal currents (**a**) and their coherent component (**b**), incoherent component (**c**) and cross-term (**d**).

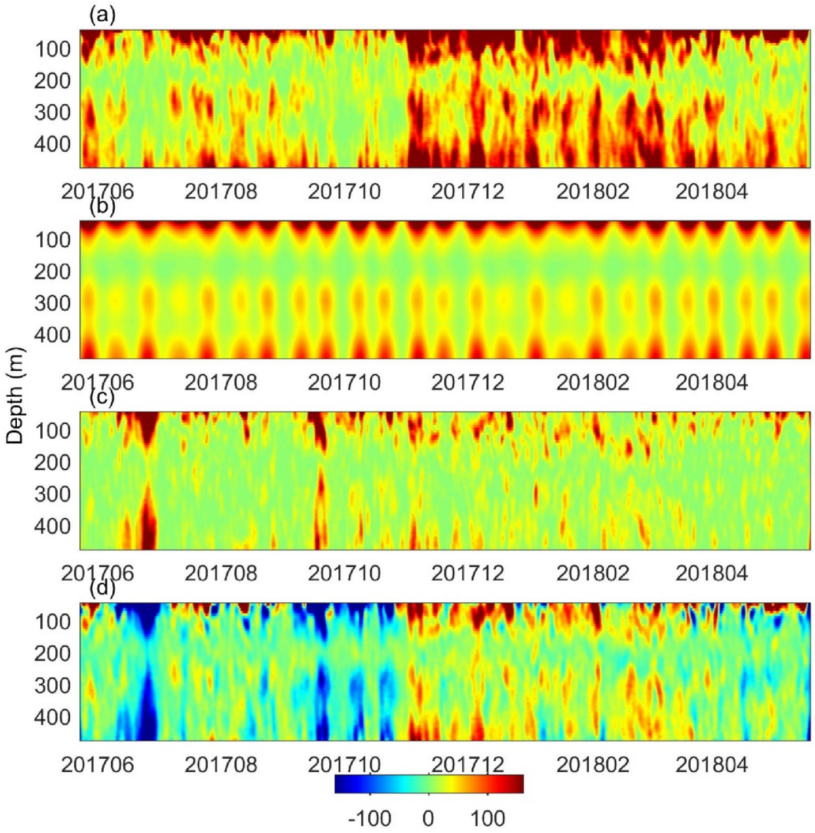

Figure 6. The HKEs (unit: J m^{-1}) of semidiurnal currents (**a**) and their coherent component (**b**), incoherent component (**c**) and cross-term (**d**).

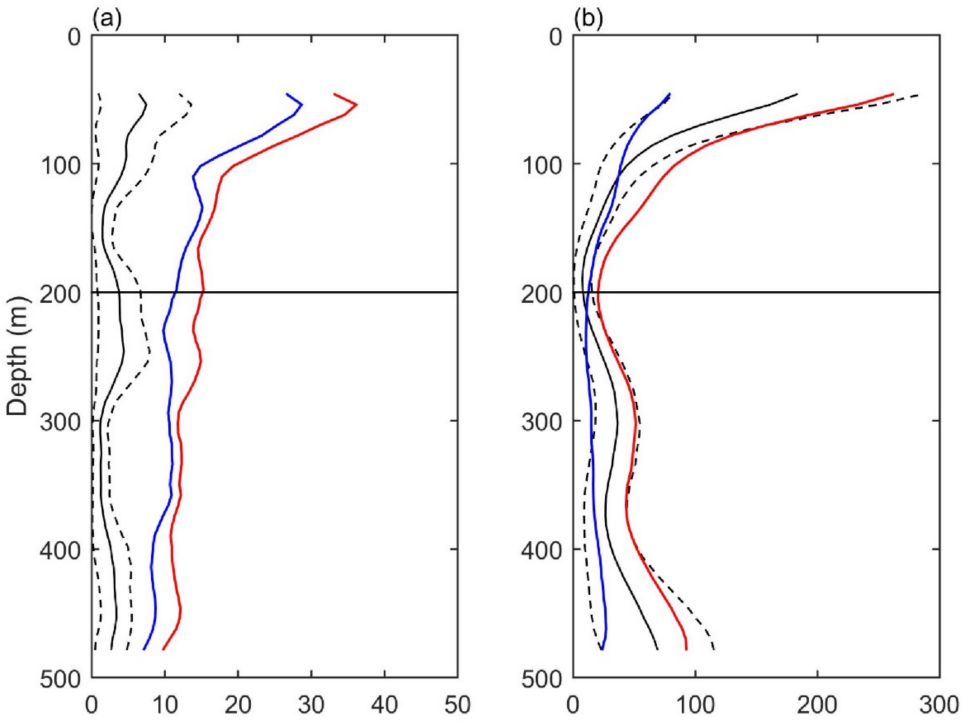

Figure 7. Mean HKEs (unit: J m^{-1}) of diurnal (**a**) and semidiurnal (**b**) currents (red lines) and their coherent component (black lines, where dashed lines represent one standard deviation) and incoherent (blue lines) component.

There was an apparent seasonal variability in the total HKE for the semidiurnal internal tides (Figure 6a). Generally, the total HKE were stronger from November to April than for the rest of the year. The mean HKE from November to April was approximately twice that from May to October. Obviously, the HKE seasonal variability was mainly due to its cross-term (Figure 6d). The mean HKE_{cr} was a quarter of the mean HKE during November to April, and the mean HKE_{cr} from November to April was equal to minus the mean value from May to October. Based on the same mooring observation, Zhao et al. [56] attributed the seasonality of semidiurnal internal tide energy to the seasonal Kuroshio onshore intrusion, which modulated the internal generation induced by the interaction of the barotropic tide and the shelf break. However, since the mooring observation only lasted for one year, the above seasonal variability in the HKEs for semidiurnal internal tides needs further verification through long-term observations.

With a 5-day low-pass filter, the power spectrum density of the depth-averaged HKEs of the diurnal and semidiurnal currents was estimated (Figure 8). In addition to the tidal oscillation, there was also significant energy at approximately 14 days and 30 days. The 13.65-day period of coherent diurnal internal tides could be attributed to the aliasing of the K_1 and O_1 constituents. The 14.84-day period of the coherent semidiurnal internal tides could be attributed to the aliasing of the M_2 and S_2 constituents, while the 28.44-day period could be attributed to the aliasing period of the M_2 and N_2 constituents. In addition, the HKE coherent component for the diurnal internal tides also showed a 170-day period, which was the aliasing period of the K_1 and P_1 constituents. This period was not significant because of the insufficient observations. The incoherent components showed some energy from the 30 to 60 day periods, which may be induced by the background current variation. It is worth noting that there were conspicuous peaks from 100 to 200 days for the depth-averaged total HKE of the semidiurnal current (Figure 8e), which were due to the HKE cross-term (Figure 8h). However, they were lower than the 95% confidence level, and not significant.

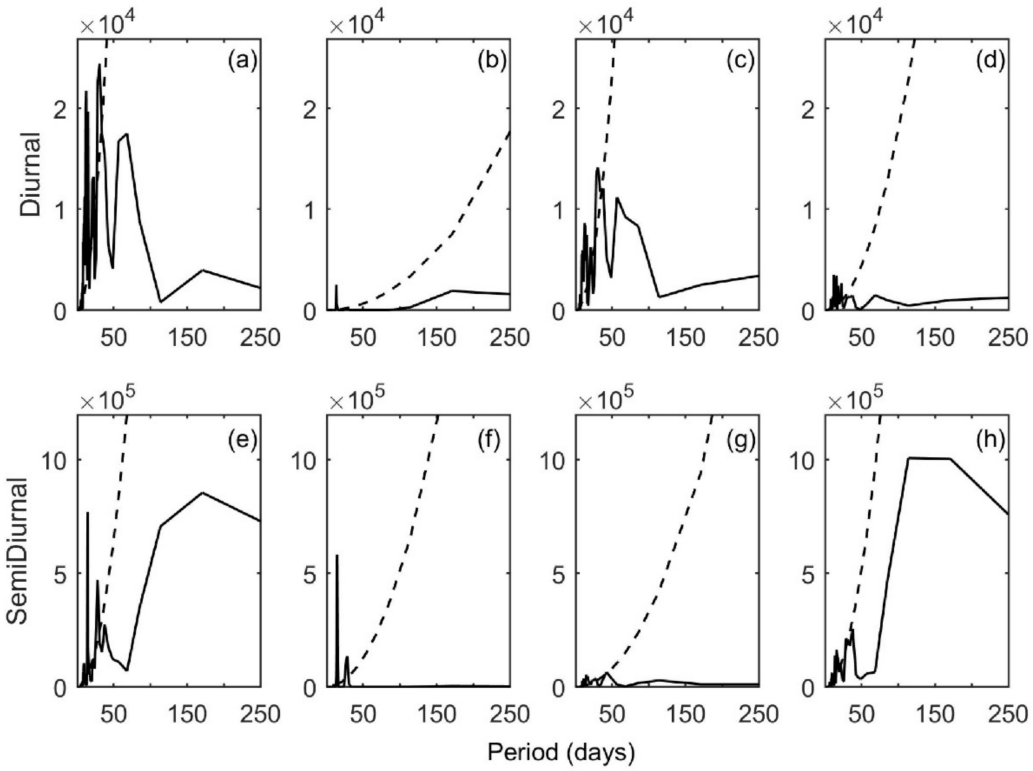

Figure 8. Power spectrum density of the depth-averaged HKEs of diurnal (**a**) and semidiurnal (**e**) currents and their coherent component (**b**,**f**), incoherent component (**c**,**g**) and cross-term (**d**,**h**). The dashed line represents the 95% confidence level.

4. Discussion

Using the one-year continuous in situ velocity observations, the vertical structure and multitemporal scale variability in the internal tides were revealed at the mooring station. The above results showed that the semidiurnal tide, especially the M_2 constituent, was dominant. In addition to the tidal oscillation and aliasing period, the semidiurnal current also showed conspicuous energy on the intraseasonal time scale (>70 days). The one-year observation served as valuable data that were able to reveal the intraseasonal variation in the internal tides. The reason that the intraseasonal variation in the HKEs was lower than the 95% confidence level could be attributed to the limited observation time period. The mooring observation (1 year) was only able to cover about three cycles of such intraseasonal oscillation.

However, the conspicuous energy from 100 to 200 days for the HKEs of the semidiurnal current was consistent with the remarkable intraseasonal variation of the Kuroshio and its onshore intrusion northeast of Taiwan Island [47,57]. Previous studies have proved that the intraseasonal variation of the geostrophic current northeast of Taiwan Island is induced by the Kuroshio being modulated by open ocean mesoscale eddies east of Taiwan Island [46,47]. The background current and ocean stratification could affect the generation and evolution of internal tides. Therefore, the one-year observation period also offers a valuable chance to estimate the impacts of the Kuroshio Current and mesoscale eddies on internal tides. The following discussion mainly focuses on the intraseasonal variation in semidiurnal internal tides and its possible mechanism. The coherent and incoherent component contributions to the total HKE of internal tides were always positive (Equations (7) and (8)). For the cross-term, the contribution was positive when the angle between the incoherent and coherent currents was smaller than 90°, and the contribution was negative when the angle was larger than 90°. Based on the HKE power spectrum density and its disciplines (Figure 8), the HKE cross-term was the main factor that gave rise to the intraseasonal variation in the semidiurnal current. The HKE incoherent component only showed a small amount of energy on the intraseasonal time scale. In terms of correlation (20-day low-pass filtered), there was no correlation between the total HKE and HKE_i, while the correlation coefficient between the total HKE and HKE_{cr} was 0.83 with no time lag (Figure 9a). The HKE cross-term was the result of the incoherent component of the internal tide, which was caused by the variation in the background current field and ocean stratification.

4.1. The Effect of Background Currents on Energy Propagation

The background currents were defined as the low frequency depth-averaged currents. With a 20-day low-pass filter, the correlation between the HKEs and in situ velocities (Figure 9b) was estimated. There was a positive correlation between the depth-averaged HKEs and velocities (Table 2, Figure 10a), meaning that a stronger background current corresponded to a higher HKE. Significantly, the correlation coefficients between the HKEs and meridional and along-shelf velocities were higher and remarkable.

Table 2. Correlation coefficient between HKEs and factors.

	Zonal Velocity	Meridional Velocity	Along-Shelf Velocity	Cross-Shelf Velocity	Kuroshio Intensity	Kuroshio Center
HKE	0.39	0.73	0.69	0.23	−0.76 (10.88 d)	−0.68 (6.25 d)
HKE_{cr}	0.26	0.72	0.65	0.40	−0.73 (12.58 d)	−0.67 (2.67 d)

The HKEs and velocities were depth-averaged and then filtered with a 20-day low-pass filter.

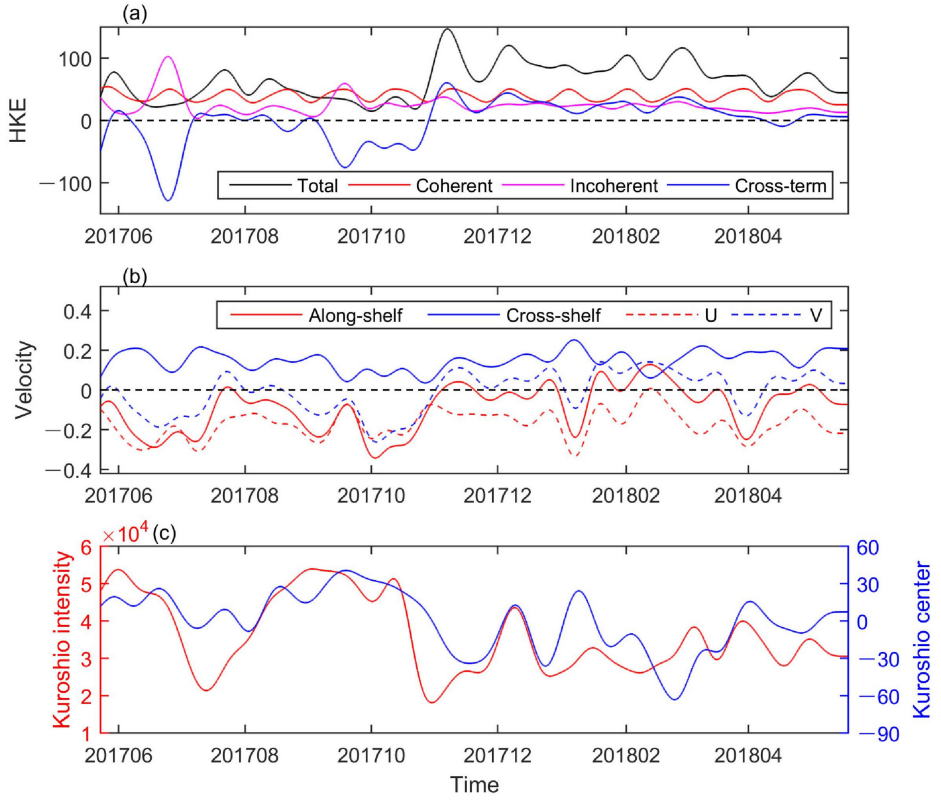

Figure 9. (**a**) Depth-averaged HKEs (unit: J m^{-1}) of semidiurnal currents and its coherent component, incoherent component and cross-term. (**b**) Depth-averaged along-shelf (50° from north), cross-shelf (310° from north), zonal and meridional velocities (unit: m s^{-1}) from 46 m to 478 m. (**c**) Kuroshio intensity (red line, unit: m^2 s^{-1}) and Kuroshio center anomaly (blue line, unit: km). All the time series were filtered with a 20-day low-pass filter.

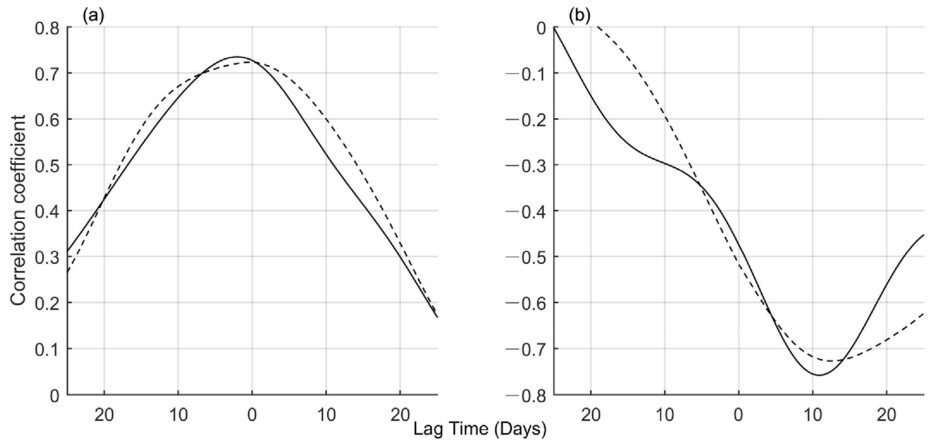

Figure 10. (**a**) Lag correlation between the depth-averaged HKEs and meridional velocities. (**b**) Lag correlation between the depth-averaged HKEs and Kuroshio intensity. The solid lines represent the total HKE, and the dashed lines represent the HKE cross-term.

First, the observed [26] and simulated [3] results showed that the direction of internal tidal energy flux around our mooring site was offshore. The Kuroshio onshore intrusion was found to inhibit offshore energy propagation and raise the energy at the observation site. This finding was consistent with the positive correlation between the HKE_{cr} and cross-shelf velocities. In their study, Rainville and Pinkel [58] also proposed that the Kuroshio Current was a barrier that impeded the seaward propagation of internal waves.

Second, the Mien-Hua Canyon has been found to be a major energy source for internal tides, and the M_2 barotropic-to-baroclinic conversion rate was ~2.35 GW [3]. The source area was very close to the mooring site (~30 km; Figure 1b); therefore, the background currents were similar. The remarkable correlation between the HKEs and along-shelf velocities indicated that the strengthened northeastward background current favoured more internal tidal energy propagation to the mooring site. Moreover, since the correlation between the HKEs and along-shelf velocities was significantly higher than the cross-shelf velocity, this explanation should be relatively more important.

4.2. The Effect of Ocean Stratification on Energy Generation

Since there were no synchronous thermohaline records for velocity at the mooring station, the daily HYCOM analysis output during the observation period was analysed to reveal the variation in ocean stratification. The analysed data assimilated the available observations, including satellite altimeters and in situ temperature and salinity profiles. The data have performed well in the research area, including for current intraseasonal variation [47,59]. An abnormal HKE_{cr} was defined as events exceeding 0.75 standard deviations (std) of the time series (20-day low-pass filtered, Figure 11a). The abnormally low HKE_{cr} occurred before November 2017, while the abnormally high HKE_{cr} occurred after November 2017. This difference occurred because the mean HKE_{cr} showed an obvious increase (~50 J m^{-1}) after November 2017. However, because of the impact of the seasonal migration of the Kuroshio Current, there is a strong seasonal cycle of stratification around the slope region [54]. A comparison of stratifications between the periods of abnormally high and low HKE_{cr} should show the seasonal variation instead of the intraseasonal variation, and that these are not reasonable. Therefore, in this study, the stratification variations during the warm period (from 12 June 2017 to 25 October 2017) and cold period (from 31 October 2017 to 10 March 2018) were analysed.

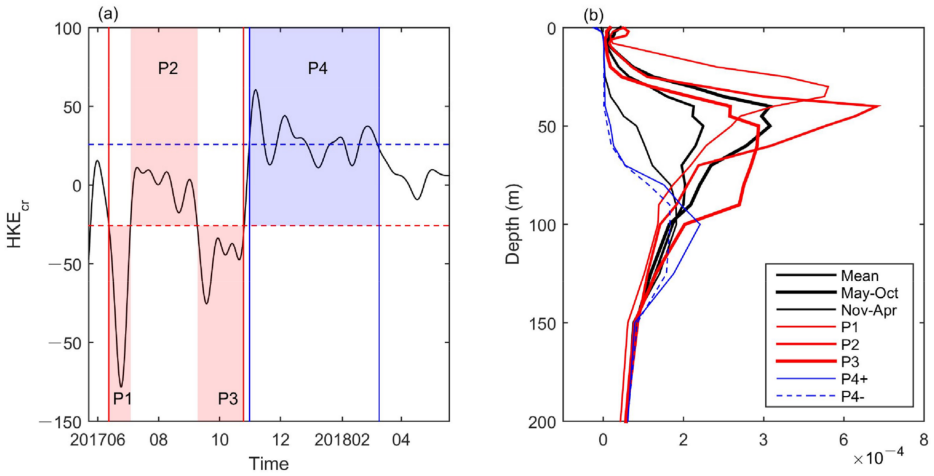

Figure 11. (**a**) Depth-averaged HKE_{cr} (20-day low-pass filtered, unit: J m^{-1}). The red (blue) dashed line represents the -0.75 (0.75) stds of the time series. The red solid lines represent the warm period (from 12 June 2017 to 25 October 2017), and the blue solid lines represent the cold period (from 31 October 2017 to 10 March 2018). P1, P2, P3 and P4 represent the periods from 12 June 2017 to 4 July 2017, from 5 July 2017 to 9 September 2017, from 10 September 2017 to 25 October 2017 and from 31 October 2017 to 10 March 2018, respectively. (**b**) Profiles of the mean Brunt-Väisälä frequency squared (unit: s^{-2}) at the mooring location derived from HYCOM analysis data. 'Mean' represents the mean value during the whole observation period; 'May-October' represents the mean value from May 2017 to October 2017; 'November-April' represents the mean value from November 2017 to April 2018; 'P1', 'P2' and 'P3' represent the mean value during the P1, P2 and P3 periods, respectively; 'P4+' ('P4−') represents the mean value when the HKE_{cr} was larger (lower) than 0.75 stds during the P4 period.

First, abnormally low HKE_{cr} events occurred in the P1 (-79.79 J m^{-1}) and P3 (-46.9 J m^{-1}) periods (Figure 11a). The buoyancy frequency (N^2) derived from the HYCOM analysis data indicated that the stratifications during the P1 (maximum was 5.61×10^{-4} s^{-2}) and P3 (maximum was 3.87×10^{-4} s^{-2}) periods were both weaker than those during the P2 (maximum was 6.81×10^{-4} s^{-2}) period (Figure 11b). In the cold period, the stratification of abnormally high HKE_{cr} events (P4+, maximum was 2.41×10^{-4} s^{-2}) was stronger than that of the rest time (P4−, maximum was 1.66×10^{-4} s^{-2}). On the intraseasonal time scale, stronger stratification favoured higher HKE_{cr}. The buoyancy frequency changed the barotropic-to-baroclinic conversion rate, which modulated the internal tide generation.

Second, internal tide generation depends on both the density gradient and topography slope [38]. At the P transect, because of the Kuroshio Current, the tilting thermocline clung to the shelf break (Figure 12). The isopycnals became more parallel to the slope with an abnormally low HKE_{cr} (during P1 and P3 period), which resulted in a weaker interaction between the stratification and topography and a decreased HKE. However, there was little difference in the isopycnals during the P4 period (Figure 12c).

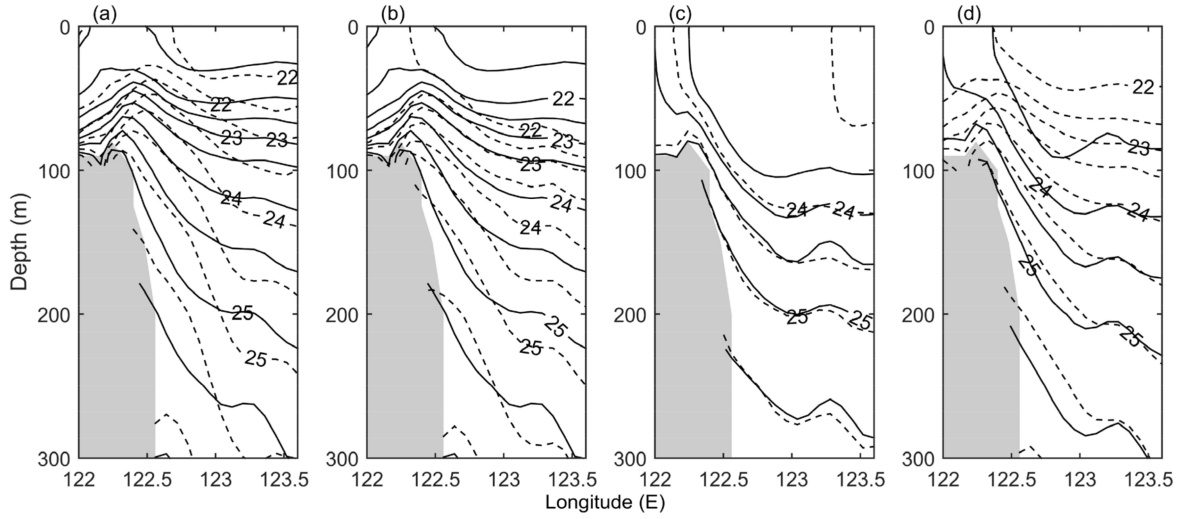

Figure 12. Mean potential density (unit: kg m^{-3}) along the P transect (**a**) during the P1 (dashed lines) and P2 (solid lines) periods, (**b**) during the P2 (solid lines) and P3 (dashed lines) periods, (**c**) during the P4+ (solid lines) and P4− (dashed lines) periods and (**d**) from May 2017 to October 2017 (solid lines) and from November 2017 to April 2018 (dashed lines).

4.3. The Effect of the Kuroshio Current and Mesoscale Eddies

At the intraseasonal time scale, previous studies showed that the current northeast of Taiwan Island was strongly influenced by the Kuroshio Current [46,47]. The sea surface level, sea surface temperature and chlorophyll-a concentration derived from satellite data performed well over China's seas and the adjacent ocean [45,60–62]. Using synchronous satellite altimetry data, both the intensity and the center of Kuroshio Current were estimated (Figure 9c). The Kuroshio intensity was defined as $\int_{X_W}^{X_E} V_g(x,t)dx$ [63], and the Kuroshio center was defined as $\frac{\int_{X_W}^{X_E} V_g(x,t)\cdot x dx}{\int_{X_W}^{X_E} V_g(x,t)dx}$ [48], where X_E and X_W are the eastern and western points of the selected transect, respectively, and V_g is the northeastward geostrophic velocity normal to the transect. The Kuroshio center was estimated at the P transect (Figure 1a). Instead of the P transect, the Kuroshio intensity was estimated at the ETC transect for convenience (solid boundaries on both sides of the Kuroshio). Due to the strong Kuroshio Current, most signals propagate downstream along the Kuroshio. Therefore, there should be a short time lag between the Kuroshio intensity and the Kuroshio center in this study.

With a 20-day low-pass filter, the relationship between the HKEs of internal tides and the Kuroshio Current was evaluated (Figure 10b). There was a significant negative

correlation (−0.76) between the total HKE and the Kuroshio intensity at a 10.88-day lag, and also a significant negative correlation (−0.73) between the HKE_{cr} and the Kuroshio intensity at a 12.58-day lag. The negative correlation between the HKEs and the Kuroshio center was also remarkable but with a shorter time lag. In general, increases in HKE occurred after a weaker Kuroshio Current, and vice versa.

The onshore (offshore) Kuroshio migration could increase (decrease) the northeastward velocity northeast of Taiwan Island [64,65]. In this study, the correlation coefficient between the depth-averaged meridional (along-shelf) velocities and the Kuroshio intensity was −0.74 (−0.69) at a 13.88-day (11.46-day) lag. The weaker (stronger) Kuroshio Current led to the westward (eastward) migration of onshore intrusion, and increased (decreased) the cross-shelf velocities at the mooring site [47,66]. The velocity increase (decrease) induced by the Kuroshio Current could enhance (weaken) the HKEs of internal tides by influencing tidal energy propagation, as we discussed previously. On the other hand, the weaker (stronger) Kuroshio Current resulted in gentler (steeper) isopycnals across the slope and enhanced (weakened) the HKEs of internal tides by influencing the interaction between the stratification and topography.

To study the reason for the Kuroshio variation, the mean sea level anomalies during periods P1, P2, P3, P4+ and P4− were composited in the research area (Figure 13). Generally, the Kuroshio Current, indicated by the sea level anomaly difference ($SLA_{offshore}$ minus $SLA_{onshore}$) across the P transect, increased during the P1 (0.17 m) and P3 (0.15 m) periods and decreased during the P4+ (−0.14 m) and P4− (−0.18 m) periods. These sea level anomalies that influenced the Kuroshio were tracked to the open ocean east of Taiwan Island, which was revealed from sea level anomalies 30 days before. Furthermore, two anticyclonic eddies and one cyclonic eddy was found east of Taiwan Island (Figure 13f–h). Anticyclonic (cyclonic) eddies could increase (decrease) the Kuroshio and migrate the Kuroshio offshore (onshore), as well as weaken (enhance) the shoreward intrusion northeast of Taiwan Island [47,64]. Therefore, in the warm period, mesoscale eddies modulated the ocean circulation and stratification at the shelf break and affected the HKEs of the internal tides. However, in the cold period, there was no obvious difference in the distribution of sea level anomalies, which may be due to the small amplitudes of HKE_{cr} within this period.

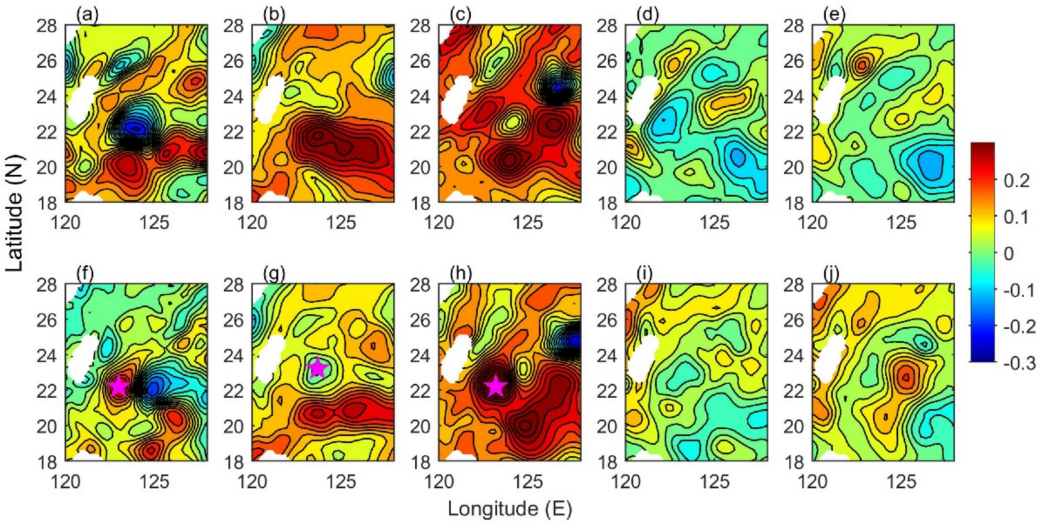

Figure 13. Mean sea level anomalies (unit: m) during the P1 (**a**), P2 (**b**), P3 (**c**), P4+ (**d**) and P4− (**e**) periods. Mean sea level anomalies 30 days before the P1 (**f**), P2 (**g**), P3 (**h**), P4+ (**i**) and P4− (**j**) periods. The contour interval is 0.03 m. The pentagram marks the location of the mesoscale eddy.

5. Conclusions

One year of continuous mooring observations provided valuable data capable of illustrate the vertical structure of and intraseasonal variability in the internal tides in the

slope region northeast of Taiwan Island. At the mooring site, the semidiurnal signal was dominant in both the barotropic and baroclinic tides, and the diurnal signal had a secondary influence. The M_2 tide was the strongest barotropic tidal constituent, and its inclination was generally consistent with the cross-isobath direction. Generally, the amplitudes of the major constituents of the internal tides were largest at ~50 m, and first decreased and then increased with depth. The M_2 tide was also the strongest internal tidal constituent. The amplitude of this tidal constituent was largest (23.66 cm s^{-1}) at 46 m, decreased to 5.2 cm s^{-1} at 190 m and increased to 15.6 cm s^{-1} at 478 m. The coherent component of HKE accounted for 62.6% of semidiurnal internal tides, while the incoherent component accounted for 37.4%. In addition to the aliasing periods, there was conspicuous energy from 100 days to 200 days for the depth-averaged total HKE of the semidiurnal internal tides. The HKE power spectrum density and its disciplines showed that the HKE cross-term was the main factor that gave rise to the intraseasonal variation in the semidiurnal current.

The intraseasonal variation in HKEs was attributed to the variations in the background current and stratification. Based on the correlation between the HKEs and the strength of the background current, two mechanisms for the variation in HKE can be proposed: First, the Kuroshio onshore intrusion could inhibit offshore energy propagation and raise the energy at the observation site; second, the strengthened northeastward background current favoured more internal tidal energy propagation from the Mien-Hua Canyon. Moreover, the higher and remarkable correlation between the HKEs and along-shelf velocities indicated that the latter mechanism should be more important. Two mechanisms can also be proposed for the stratification: First, a larger buoyancy frequency in the upper ocean, which increased the barotropic-to-baroclinic conversion rate, enhanced the internal tide generation; second, a reduction in the slope of isopycnals in the slope region resulted in a stronger interaction between the stratification and topography and increased the HKE.

The cyclonic (anticyclonic) mesoscale eddies east of Taiwan Island weakened (strengthened) the Kuroshio, and shifted the Kuroshio onshore (offshore) northeast of Taiwan Island. The weakened (strengthened) Kuroshio increased (decreased) the cross-shelf velocities at the mooring site, and the onshore (offshore) Kuroshio migration increased (decreased) the northeastward velocities and enhanced (weakened) the HKEs of the internal tides by modulating the tidal energy horizontal propagation. The weakened (strengthened) Kuroshio resulted in gentler (steeper) isopycnals across the slope and enhanced (weakened) the HKEs of the internal tides by influencing the interaction between the stratification and topography.

In addition, although one year of observations were insufficient, the seasonal variation in the HKEs of the internal tides was also discussed. The HKEs were stronger in winter than in summer (Figure 9a). The Kuroshio Branch Current and onshore intrusion northeast of Taiwan Island were stronger in winter [54,67]. However, due to strong surface cooling, the buoyancy frequency in the upper ocean was weakened (Figure 11b), and the isopycnals were steeper (Figure 12d). The stratification variation contradicted the stronger HKEs. Therefore, the enhanced HKEs in winter should be attributed to the increased velocities induced by the Kuroshio.

The findings of this work will contribute toward a better understanding of the intraseasonal variation of internal tides northeast of Taiwan Island. The results also could provide reference for improvement of the parameterization of ocean turbulence in numerical simulation, as well as for the high-resolution numerical forecasting of coastal environments. However, the investigation of the internal tides is very limited with only current velocities at one single station. In the following study, we will try to combine in situ observation and high-resolution numerical simulation to study the generation and dissipation of the internal tides northeast of Taiwan Island, as well as the impact of Kuroshio Current on them.

Author Contributions: Conceptualization, Y.Y.; methodology, X.L. and Y.Y.; software, Q.C.; validation, Z.L. and Y.Y.; formal analysis, Y.Y.; investigation, X.Z.; resources, Y.H.; data curation, Z.L.; writing—original draft preparation, Y.Y.; writing—review and editing, Z.L. and Y.Z.; visualization,

Y.Y.; supervision, Z.L.; project administration, Y.Y. and Y.H.; funding acquisition, Y.Y., Z.L., Y.Z. and Y.H. All authors have read and agreed to the published version of the manuscript.

Funding: The research was funded by the National Natural Science Foundation of China, grant number 42076002, 41630967, 41776020 and U1901215, and the Strategic Priority Research Program of the Chinese Academy of Sciences, grand number XDB42000000.

Institutional Review Board Statement: Not applicable.

Informed Consent Statement: Not applicable.

Data Availability Statement: The mooring data presented in this study are available from the corresponding author upon reasonable request. The gridded satellite altimetry data, including sea level heights and currents are available from the Copernicus Marine Environment Monitoring Service (CMEMS, https://marine.copernicus.eu, accessed on 21 November 2021). The synchronous ocean analysis data are available from the data server of HYCOM (https://www.hycom.org/data/glbu0pt08/expt-91pt2, accessed on 21 November 2021).

Acknowledgments: The acquisition of mooring data was supported by the NSFC Open Research Cruise (Cruises Nos. NORC2017-01, NORC2017-02 & NORC2018-01), funded by the Ship-time Sharing Project of NSFC. This cruise was conducted onboard R/V "Xiang Yang Hong 18" by the First Institute of Oceanography, State Oceanic Administration, China.

Conflicts of Interest: The authors declare no conflict of interest.

References

1. Baines, P. On internal tide generation models. *Deep. Sea Res. Part A Oceanogr. Res. Pap.* **1982**, *29*, 307–338. [CrossRef]
2. Garrett, C.; Kunze, E. Internal Tide Generation in the Deep Ocean. *Annu. Rev. Fluid Mech.* **2007**, *39*, 57–87. [CrossRef]
3. Chang, H.; Xu, Z.; Yin, B.; Hou, Y.; Liu, Y.; Li, D.; Wang, Y.; Cao, S.; Liu, A.K. Generation and Propagation of M 2 Internal Tides Modulated by the Kuroshio Northeast of Taiwan. *J. Geophys. Res. Oceans* **2019**, *124*, 2728–2749. [CrossRef]
4. Wunsch, C.; Ferrari, R. Vertical mixing, energy, and the general circulation of the oceans. *Annu. Rev. Fluid Mech.* **2004**, *36*, 281–314. [CrossRef]
5. Nagai, T.; Hasegawa, D.; Tanaka, T.; Nakamura, H.; Tsutsumi, E.; Inoue, R.; Yamashiro, T. First Evidence of Coherent Bands of Strong Turbulent Layers Associated with High-Wavenumber Internal-Wave Shear in the Upstream Kuroshio. *Sci. Rep.* **2017**, *7*, 14555. [CrossRef]
6. Cimoli, L.; Caulfield, C.P.; Johnson, H.L.; Marshall, D.P.; Mashayek, A.; Garabato, A.N.; Vic, C. Sensitivity of Deep Ocean Mixing to Local Internal Tide Breaking and Mixing Efficiency. *Geophys. Res. Lett.* **2019**, *43*, 14622–14633. [CrossRef]
7. Munk, W.; Wunsch, C. Abyssal recipes II: Energetics of tidal and wind mixing. *Deep. Sea Res. Part I Oceanogr. Res. Pap.* **1998**, *45*, 1977–2010. [CrossRef]
8. Laurent, L.S.; Garrett, C. The Role of Internal Tides in Mixing the Deep Ocean. *J. Phys. Oceanogr.* **2002**, *32*, 2882–2899. [CrossRef]
9. Williams, K.; Henyey, F.S.; Rouseff, D.; Reynolds, S.A.; Ewart, T. Internal wave effects on high-frequency acoustic propagation to horizontal arrays-experiment and implications to imaging. *IEEE J. Ocean. Eng.* **2001**, *26*, 102–112. [CrossRef]
10. Wunsch, C. Internal tides in the ocean. *Rev. Geophys.* **1975**, *13*, 167–182. [CrossRef]
11. Alford, M.H. Redistribution of energy available for ocean mixing by long-range propagation of internal waves. *Nature* **2003**, *423*, 159–162. [CrossRef] [PubMed]
12. Alford, M.H.; Gregg, M.C.; Merrifield, M.A. Structure, Propagation, and Mixing of Energetic Baroclinic Tides in Mamala Bay, Oahu, Hawaii. *J. Phys. Oceanogr.* **2006**, *36*, 997–1018. [CrossRef]
13. Zhao, Z.; Alford, M.H.; Girton, J.B.; Rainville, L.; Simmons, H.L. Global Observations of Open-Ocean Mode-1 M2 Internal Tides. *J. Phys. Oceanogr.* **2016**, *46*, 1657–1684. [CrossRef]
14. Nakamura, T.; Awaji, T. Scattering of Internal Waves with Frequency Change over Rough Topography. *J. Phys. Oceanogr.* **2009**, *39*, 1574–1594. [CrossRef]
15. Nikurashin, M.; Legg, S. A Mechanism for Local Dissipation of Internal Tides Generated at Rough Topography. *J. Phys. Oceanogr.* **2011**, *41*, 378–395. [CrossRef]
16. Niwa, Y.; Hibiya, T. Numerical study of the spatial distribution of the M2internal tide in the Pacific Ocean. *J. Geophys. Res. Space Phys.* **2001**, *106*, 22441–22449. [CrossRef]
17. Niwa, Y.; Hibiya, T. Three-dimensional numerical simulation of M2 internal tides in the East China Sea. *J. Geophys. Res. Oceans* **2004**, *109*. [CrossRef]
18. Zhao, Z.; Klemas, V.; Zheng, Q.; Yan, X.-H. Remote sensing evidence for baroclinic tide origin of internal solitary waves in the northeastern South China Sea. *Geophys. Res. Lett.* **2004**, *31*, 06302. [CrossRef]
19. Larsen, L.; Cannon, G.; Choi, B. East China Sea tide currents. *Cont. Shelf Res.* **1985**, *4*, 77–103. [CrossRef]
20. Fang, G. Tide and tidal current charts for the marginal seas adjacent to China. *Chin. J. Oceanol. Limnol.* **1986**, *4*, 1–16.

21. Li, L.; Jiang, W.; Li, P.; Yang, B. Vertical structure of the tidal currents on the continental shelf of the East China Sea. *J. Ocean Univ. China* **2012**, *11*, 347–353. [CrossRef]
22. Guo, X.; Yanagi, T. Three-dimensional structure of tidal current in the East China Sea and the Yellow Sea. *J. Oceanogr.* **1998**, *54*, 651–668. [CrossRef]
23. Da Silva, J.C.B.; New, A.L.; Srokosz, M.A.; Smyth, T. On the observability of internal tidal waves in remotely-sensed ocean colour data. *Geophys. Res. Lett.* **2002**, *29*, 10–11. [CrossRef]
24. Kuroda, Y.; Mitsudera, H. Observation of internal tides in the East China Sea with an underwater sliding vehicle. *J. Geophys. Res. Oceans* **1995**, *100*, 10801. [CrossRef]
25. Duda, T.F.; Newhall, A.E.; Gawarkiewicz, G.; Caruso, M.J.; Graber, H.C.; Yang, Y.J.; Jan, S. Significant internal waves and internal tides measured northeast of Taiwan. *J. Mar. Res.* **2013**, *71*, 47–81. [CrossRef]
26. Lien, R.-C.; Sanford, T.B.; Jan, S.; Chang, M.-H.; Ma, B.B. Internal tides on the East China Sea Continental Slope. *J. Mar. Res.* **2013**, *71*, 151–185. [CrossRef]
27. Liu, A.K.; Chang, Y.S.; Hsu, M.-K.; Liang, N.K. Evolution of nonlinear internal waves in the East and South China Seas. *J. Geophys. Res. Oceans* **1998**, *103*, 7995–8008. [CrossRef]
28. Hsu, M.-K.; Liu, A.K.; Liu, C. A study of internal waves in the China Seas and Yellow Sea using SAR. *Cont. Shelf Res.* **2000**, *20*, 389–410. [CrossRef]
29. Gerkema, T.; Lam, F.A.; Maas, L.R. Internal tides in the Bay of Biscay: Conversion rates and seasonal effects. *Deep. Sea Res. Part II Top. Stud. Oceanogr.* **2004**, *51*, 2995–3008. [CrossRef]
30. Nash, J.D.; Kelly, S.M.; Shroyer, E.L.; Moum, J.N.; Duda, T. The Unpredictable Nature of Internal Tides on Continental Shelves. *J. Phys. Oceanogr.* **2012**, *42*, 1981–2000. [CrossRef]
31. Pickering, A.; Alford, M.; Nash, J.; Rainville, L.; Buijsman, M.; Ko, D.S.; Lim, B. Structure and Variability of Internal Tides in Luzon Strait. *J. Phys. Oceanogr.* **2015**, *45*, 1574–1594. [CrossRef]
32. Klymak, J.M.; Pinkel, R.; Rainville, L. Direct Breaking of the Internal Tide near Topography: Kaena Ridge, Hawaii. *J. Phys. Oceanogr.* **2008**, *38*, 380–399. [CrossRef]
33. Cao, A.; Guo, Z.; Wang, S.; Chen, X.; Lv, X.; Song, J. Upper ocean shear in the northern South China Sea. *J. Oceanogr.* **2019**, *75*, 525–539. [CrossRef]
34. Xu, Z.; Yin, B.; Hou, Y.; Xu, Y. Variability of internal tides and near-inertial waves on the continental slope of the northwestern South China Sea. *J. Geophys. Res. Oceans* **2013**, *118*, 197–211. [CrossRef]
35. Du, T.; Tseng, Y.-H.; Yan, X.-H. Impacts of tidal currents and Kuroshio intrusion on the generation of nonlinear internal waves in Luzon Strait. *J. Geophys. Res. Oceans* **2008**, *113*, 08015. [CrossRef]
36. Park, J.-H.; Farmer, D. Effects of Kuroshio intrusions on nonlinear internal waves in the South China Sea during winter. *J. Geophys. Res. Oceans* **2013**, *118*, 7081–7094. [CrossRef]
37. Li, Q.; Wang, B.; Chen, X.; Chen, X.; Park, J. Variability of nonlinear internal waves in the South China Sea affected by the Kuroshio and mesoscale eddies. *J. Geophys. Res. Oceans* **2016**, *121*, 2098–2118. [CrossRef]
38. Vlasenko, V.; Stashchuk, N.; Hutter, K. *Baroclinic Tides*; Cambridge University Press: Cambridge, UK, 2005; pp. 94–100.
39. Jan, S.; Chern, C.-S.; Wang, J.; Chiou, M.-D. Generation and propagation of baroclinic tides modified by the Kuroshio in the Luzon Strait. *J. Geophys. Res. Oceans* **2012**, *117*, 02019. [CrossRef]
40. Yuan, Y.; Zheng, Q.; Dai, D.; Hu, X.; Qiao, F.; Meng, J. Mechanism of internal waves in the Luzon Strait. *J. Geophys. Res.* **2006**, *111*, C11S17. [CrossRef]
41. Xie, J.; He, Y.; Chen, Z.; Xu, J.; Cai, S. Simulations of internal solitary wave interactions with mesoscale eddies in the north-eastern South China Sea. *J. Phys. Oceanogr.* **2015**, *45*, 2959–2978. [CrossRef]
42. Li, B.; Wei, Z.; Wang, X.; Fu, Y.; Fu, Q.; Li, J.; Lv, X. Variability of coherent and incoherent features of internal tides in the north South China Sea. *Sci. Rep.* **2020**, *10*, 12904. [CrossRef]
43. Huang, X.; Zhang, Z.; Zhang, X.; Qian, H.; Zhao, W.; Tian, J. Impacts of a Mesoscale Eddy Pair on Internal Solitary Waves in the Northern South China Sea revealed by Mooring Array Observations. *J. Phys. Oceanogr.* **2017**, *47*, 1539–1554. [CrossRef]
44. Ma, B.B.; Lien, R.-C.; Ko, D.S. The variability of internal tides in the Northern South China Sea. *J. Oceanogr.* **2013**, *69*, 619–630. [CrossRef]
45. Zhang, D.; Lee, T.N.; Johns, W.E.; Liu, C.-T.; Zantopp, R. The Kuroshio East of Taiwan: Modes of Variability and Relationship to Interior Ocean Mesoscale Eddies. *J. Phys. Oceanogr.* **2001**, *31*, 1054–1074. [CrossRef]
46. Vélez-Belchí, P.; Centurioni, L.R.; Lee, D.-K.; Jan, S.; Niiler, P.P. Eddy induced Kuroshio intrusions onto the continental shelf of the East China Sea. *J. Mar. Res.* **2013**, *71*, 83–107. [CrossRef]
47. Yin, Y.; Lin, X.; He, R.; Hou, Y. Impact of mesoscale eddies on Kuroshio intrusion variability northeast of Taiwan. *J. Geophys. Res. Oceans* **2017**, *122*, 3021–3040. [CrossRef]
48. Yin, Y.; Liu, Z.; Hu, P.; Hou, Y.; Lu, J.; He, Y. Impact of mesoscale eddies on the southwestward countercurrent northeast of Taiwan revealed by ADCP mooring observations. *Cont. Shelf Res.* **2020**, *195*, 104063. [CrossRef]
49. Chelton, D.B.; Schlax, M.G.; Samelson, R.M. Global observations of nonlinear mesoscale eddies. *Prog. Oceanogr.* **2011**, *91*, 167–216. [CrossRef]
50. Rio, M.H.; Guinehut, S.; Larnicol, G. New CNES-CLS09 global mean dynamic topography computed from the combination of GRACE data, altimetry, and in situ measurements. *J. Geophys. Res. Oceans* **2011**, *116*, 07018. [CrossRef]

51. Chassignet, E.P.; Hurlburt, H.E.; Metzger, E.J.; Smedstad, O.M.; Cummings, J.A.; Halliwell, G.R.; Bleck, R.; Baraille, R.; Wallcraft, A.J.; Lozano, C.; et al. US GODAE: Global Ocean Prediction with the HYbrid Coordinate Ocean Model (HYCOM). *Oceanography* **2009**, *22*, 64–75. [CrossRef]
52. Cummings, J.A.; Smedstad, O.M. Variational Data Assimilation for the Global Ocean. In *Data Assimilation for Atmospheric, Oceanic and Hydrologic Applications*; Park, S., Xu, L., Eds.; Springer: Berlin/Heidelberg, Germany, 2013; Volume 2, pp. 303–343.
53. Chao, S.-Y. Circulation of the East China Sea, a numerical study. *J. Oceanogr.* **1990**, *46*, 273–295. [CrossRef]
54. Oey, L.-Y.; Hsin, Y.-C.; Wu, C.-R. Why does the Kuroshio northeast of Taiwan shift shelfward in winter? *Ocean Dyn.* **2010**, *60*, 413–426. [CrossRef]
55. James, C.; Wimbush, M.; Ichikawa, H. Kuroshio Meanders in the East China Sea. *J. Phys. Oceanogr.* **1999**, *29*, 259–272. [CrossRef]
56. Zhao, X.; Hou, Y.; Liu, Z.; Zhuang, Z.; Wang, K. Seasonal Variability of Internal Tides Northeast of Taiwan. *J. Ocean Univ. China* **2020**, *19*, 740–746. [CrossRef]
57. Johns, W.E.; Lee, T.N.; Zhang, D.X.; Zantopp, R.; Liu, C.T.; Yang, Y. The Kuroshio east of Taiwan: Moored transport observations from the WOCE PCM-1 array. *J. Phys. Oceanogr.* **2001**, *31*, 1031–1053. [CrossRef]
58. Rainville, L.; Pinkel, R. Observations of Energetic High-Wavenumber Internal Waves in the Kuroshio. *J. Phys. Oceanogr.* **2004**, *34*, 1495–1505. [CrossRef]
59. He, Y.; Hu, P.; Yin, Y.; Liu, Z.; Liu, Y.; Hou, Y.; Zhang, Y. Vertical Migration of the Along-Slope Counter-Flow and Its Relation with the Kuroshio Intrusion off Northeastern Taiwan. *Remote Sens.* **2019**, *11*, 2624. [CrossRef]
60. Ji, C.; Zhang, Y.; Cheng, Q.; Li, Y.; Jiang, T.; Liang, X.S. Analyzing the variation of the precipitation of coastal areas of eastern China and its association with sea surface temperature (SST) of other seas. *Atmos. Res.* **2019**, *219*, 114–122. [CrossRef]
61. Ji, C.; Zhang, Y.; Cheng, Q.; Tsou, J.; Jiang, T.; Liang, X.S. Evaluating the impact of sea surface temperature (SST) on spatial distribution of chlorophyll-a concentration in the East China Sea. *Int. J. Appl. Earth Obs. Geoinf.* **2018**, *68*, 252–261. [CrossRef]
62. Zhang, Y.; Huang, Z.; Fu, D.; Tsou, J.; Jiang, T.; Liang, X.; Lu, X. Monitoring of chlorophyll-a and sea surface silicate concen-trations in the south part of Cheju island in the East China Sea using MODIS data. *Int. J. Appl. Earth Obs. Geoinf.* **2018**, *67*, 173–178. [CrossRef]
63. Hsin, Y.-C.; Qiu, B.; Chiang, T.-L.; Wu, C.-R. Seasonal to interannual variations in the intensity and central position of the surface Kuroshio east of Taiwan. *J. Geophys. Res. Oceans* **2013**, *118*, 4305–4316. [CrossRef]
64. Ichikawa, K.; Tokeshi, R.; Kashima, M.; Sato, K.; Matsuoka, T.; Kojima, S.; Fujii, S. Kuroshio variations in the upstream region as seen by HF radar and satellite altimetry data. *Int. J. Remote Sens.* **2008**, *29*, 6417–6426. [CrossRef]
65. Tang, T.; Tai, J.-H.; Yang, Y.-J. The flow pattern north of Taiwan and the migration of the Kuroshio. *Cont. Shelf Res.* **2000**, *20*, 349–371. [CrossRef]
66. Liu, C.; Wang, F.; Chen, X.; Von Storch, J.-S. Interannual variability of the Kuroshio onshore intrusion along the East China Sea shelf break: Effect of the Kuroshio volume transport. *J. Geophys. Res. Oceans* **2014**, *119*, 6190–6209. [CrossRef]
67. Isobe, A. Recent advances in ocean-circulation research on the Yellow Sea and East China Sea shelves. *J. Oceanogr.* **2008**, *64*, 569–584. [CrossRef]